5-2007

A Study of Induced Drag and Spanwise Lift Distribution for Three-Dimensional Inviscid Flow Over a Wing

Scott Monsch
Clemson University, smonsch@clemson.edu

A STUDY OF INDUCED DRAG AND SPANWISE LIFT DISTRIBUTION FOR
THREE-DIMENSIONAL INVISCID FLOW OVER A WING

_____

A Thesis
Presented to
the Graduate School of
Clemson University

_____

In Partial Fulfillment
of the Requirements for the Degree
Master of Science
Mechanical Engineering

_____

by
Scott Christopher Monsch
May 2007

_____

Accepted by:
Dr. Richard S. Figliola, Committee Chair
Dr. Richard S. Miller
Dr. Donald E. Beasley

ABSTRACT

The purpose of this study was to validate an approach to estimating the induced drag on a finite wing by using a wake integral analysis. The long-term goal is related to developing an aerodynamic-structural systems integrated design methodology for wings through the use of a transpiration boundary condition to control the spanwise lift distribution throughout a typical aircraft mission so as to minimize lift–induced drag. The short term goal addressed by this study is to develop a methodology to extract accurate and robust calculations of the induced drag from second order numerical solutions.

Numerical results for an untwisted, finite rectangular wing (NACA 0012, AR = 6.7) using no flap deflections are compared against theoretical lifting line predictions. The numerical approach used an Euler-based computational fluid dynamic (CFD) solver. An in-house lifting line code was used to predict the theoretical reference values. By dividing the wing into twenty span-wise sections and using a surface integral of pressure at each section, a span-wise lift distribution was extracted from the CFD solution. Under flow conditions representing subsonic and transonic flows (Mach 0.3 – 0.7) at small angles of attack, the comparison between the predicted numerical and lifting-line span-wise lift distributions show good agreement with a maximum deviation of only 2.4% over the wing span.

The induced drag was extracted from the downstream wake using a wake integral technique referred to as Trefftz plane analysis. This approach was attempted because (1) there are known inherent inaccuracies associated with using the more common surface integral method for calculating the drag of a wing, and (2) the wake integral approach

directly isolates the induced drag from other drag (viscous and wake) components. The predictions for induced drag based on surface integration, wake integration and lifting line methods are compared. The numerical induced drag results show a dependency on the downstream location of the Trefftz plane. Near wake and compressible flow corrections were applied to improve the induced drag predictions by wake integration. The wake integration approach is susceptible to artificial dissipation due to the numerical flow grid used, which provides an error that increases as the position of the Trefftz plane moves further downstream. Attempts to estimate the extent of this effect and to correct for it are discussed.

The numerical solution of the Euler equations demonstrates successful implementation of the wake integral method via a Trefftz Plane analysis of the induced drag. The study details an initial effort to identify and to quantify the numerical uncertainties associated with the simulation and, specifically, the induced drag prediction.

ACKNOWLEDGEMENTS

TABLE OF CONTENTS

Table of Contents (Continued)

LIST OF FIGURES

NOMENCLATURE

A	Area
A	Axial force
AR	Aspect ratio
a	Speed of sound
b	Span length
c	Chord length
C_{Di}	Coefficient of induced drag
C_L	Lift force coefficient
C_l	Section lift force coefficient
C_p	Pressure coefficient
D	Drag force
D_i	Induced drag
D_p	Profile drag
e	Specific energy per unit volume
F_s	Factor of safety
H	Total Enthalpy
h	Enthalpy
k	Thermal conductivity
LE	Leading edge
L	Section lift force
M	Mach number
N	Normal force
$\hat{\mathbf{n}}$	Normal vector
P	Static pressure
q	Dynamic pressure
R	Gas constant
r	Grid refinement ratio
S	Total surface area
s	Entropy
T	Static temperature
t	Airfoil thickness
t	Time
TE	Trailing edge
U	Uncertainty
U	Velocity
u	Component of velocity in the x-direction
V	Volume
v	Component of velocity in the y-direction
W	Conservative Variables
w	Component of velocity in the z-direction

Nomenclature (Continued)

w	Downwash velocity
α	Geometric angle of attack
α_ε	Effective angle of attack
α_{ol}	Zero-lift angle of attack
$\in$	Downwash angle
Γ	Circulation
μ	Viscosity
ρ	Density
Θ	Angle
∞	Freestream conditions

CHAPTER 1

INTRODUCTION

Modern aircraft wings are simple structures that enable heavier-than-air vehicles to take flight. In the first hundred years of powered flight, aircraft wings evolved and became more efficient with each decade. The structural design of the wings changed from bi-plane and tri-plane designs, with external supports and mechanical rigging for the wing, to monoplane designs with internal mechanisms and supports. A variety of mechanical systems were adopted for aerodynamic control. These included flaps, slats, ailerons, and spoilers. Wings also became fuel tanks, antennas, and payload carriers, in addition to the prime devices used for generating lift. Wings continued to evolve geometrically by incorporating taper, winglets, and sweep to improve aerodynamic efficiency. It is anticipated that aircraft wings will continue to evolve in the second century of flight to allow the wing to adapt to best meet the needs for a particular flight segment [1]. Adaptive-surface flow control is one of the technologies that will contribute to this evolution. The integration of adaptive control surfaces into aircraft designs will allow wings to actively respond to their environment either to enhance performance or to improve efficiency. Whether the airplane is taking-off, ascending, cruising, descending, loitering, or landing, this technology will allow a wing to tailor its shape to achieve optimal flight conditions.

Generally, aircraft design engineers optimize such a conventional flight vehicle's wings for a specific flight condition or set of conditions. Design optimizations, however,

often do not consider aerodynamic efficiency. Different criteria pertinent to a vehicle's mission are the primary concern in these design optimizations. An aircraft mission could demand that a vehicle have traits that give it enhanced speed, stealth, maximum loiter, endurance, range, maneuverability, high wing loading, survivability, stability, high ceiling, or a combination of these. Often, highly constrained design optimizations have a negative impact on overall aerodynamic effectiveness. Conventional wing designs are often optimized for specific mission criteria, so some designs tend to be inadequate during off-design flight regimes that are not associated with the aircraft's overall purpose. Designers typically incorporate mechanical systems such as slats, spoilers, and flaps into wing designs to mitigate the design deficiencies in the off-design flight regimes. Despite the design improvements in the first century of powered flight, conventional wings lacked flexibility to adapt to unknown or changing flight conditions. With recent advances in both material sciences and electro-mechanical systems research, adaptive control surface technology can now be incorporated into wing designs. Previously, such systems were impractical because size, cost, and weight offset their benefits. Now with smaller, more powerful, inexpensive, and energy efficient sensors, control systems, and actuators, adaptive control surfaces are becoming a reality both in dynamic wind tunnel models and flight test vehicles. The power of modern numerical methods can be leveraged through computational fluid dynamics (CFD) to solve for steady and transient flow conditions as a means for benchmarking and testing this technology. It has the potential to reveal any problems with aircraft aerodynamics before a single component is constructed. With this vision in mind, this study looks at a method to enable the

numerical modeling of the aerodynamic effects of adaptive trailing edge control within a design capable environment.

The inspiration for the chosen approach comes from the pioneering work by Kolonay, Eastep, and Sanders [2] on active conformal control surfaces utilized to explore the issue of inflexibility in conventional designs. In their study, they simulated active conformal control surfaces to tailor the spanwise lift distribution of a given wing to a desired shape and subsequent control of the drag induced by the tip vortices. Their study employed a lattice vortex method coupled with a generic optimizer to yield an elliptical spanwise lift distribution using trailing edge controls. This promising effort inspired further development of the work. This study represents an extension of the Kolonay et al [2] approach by using a three-dimensional unstructured finite-volume solver and transpiration boundary conditions to facilitate CFD-based optimization studies. The use of an inviscid flow solver is the logical next course in this research because the inviscid solver has a higher fidelity than the vortex lattice method used by Kolonay et al [2]. Unlike a panel method or a potential flow solver, an Euler code does not require a priori knowledge of a wake's geometry [3]. Moreover, an Euler solver serves as a good transition because it has less of a computation overhead than a Navier-Stokes flow solver. This results from not having to compute the viscous fluxes. Lift-induced drag is independent of fluid viscosity; it is an artifact from the formation of the trailing edge vortices which are by-products of the pressure difference used to generate lift [4]. This is why the viscous terms of the governing equations of fluid mechanics can be neglected.

Transpiration boundary conditions impose a velocity component normal to a wing section in a manner such that the instantaneous tangential velocity component at that

section takes on the same value that would exist with a physical geometric surface deflection, such as the deflection of a flap. The successful use of transpiration boundary conditions would overcome a major hurdle of computational complexity and time when using high fidelity CFD methods by circumventing the need to re-grid and test the flow domain with each geometric variation. As such, it enables the CFD code to be used efficiently particularly when coupled with other time-intensive numerical predictors, such as structural codes and geometry optimizers, within a design environment.

The focus of this thesis is on the methodology used to extract both the spanwise lift distribution and the induced drag from the CFD solution, and to identify potential elements of error, as well as to quantify those errors through an uncertainty analysis. At present, drag over a finite wing can be extracted from a numerical flow solution via two methods: a surface integration or a farfield analysis. The surface integration method is elementary by design and simply gives a mechanical breakdown of the forces acting on the wing into its normal component (pressure) and its tangential component (friction). However, this method has proven to be relatively inconsistent at predicting drag [5], especially with reasonable mesh sizes. With this noted deficiency in mind, the latter method will be used in this study which, although requiring more computational resources during the post-processing phase, allows "a phenomenological breakdown of drag into its physical components (lift-induced drag, wave drag, and with the Navier-Stokes equations, viscous drag)" [6]. While this delineation of drag into its components is attractive, the farfield method is not without issues of its own. Numerical methods, and the grids associated with them, give rise to spurious sources of drag that affect the induced drag prediction. In farfield methods, the induced drag estimate, which should be

4

a constant for a wing configuration and flight condition, is found to decrease as the location of analysis is moved further downstream [3]. However, with appropriate analysis of the solution field, Bourdin shows that these errors can be identified, estimated, and potentially eliminated.

The global objective of the project, of which this study is but one part, is to achieve a closed loop abstract control system by coupling flow solver code with a structural optimization program in a design capable environment. We envision that multiple virtual trailing edge control surfaces will be used to change the span-wise lift distribution of a finite wing within an Euler solver. The manipulation of the lift distribution by these virtual control surfaces will cause a change in lift-induced drag which will show up in the farfield analysis, thus allowing optimization of the lift distribution for specific needs such as minimum induced drag. This larger objective will require the transitioning of methodologies and techniques developed in the post-processing stage of analysis directly into the flow solver. Only then can the flow solver's link to an optimization routine be constructed, and the control loop closed.

CHAPTER 2

LITERATURE REVIEW

Over the past century and since the realization of powered flight, the study of drag has remained a primary focus of aircraft research and design. Drag is an essential design criterion that affects a multitude of capabilities including, but certainly not limited to, top speed, range, and fuel consumption. At cruise, generally the greatest portion of any flight, Kroo [7] estimates that lift induced drag accounts for approximately 40% of the total drag for a typical transport aircraft. At lower speeds, and especially at takeoff, lift induced drag can account for as much as 80-90% of the total drag. Kroo argues that although takeoff is arguably very short when compared to the total duration of flight, "it's influence on the overall aircraft design is profound." He goes on to note, "that it remains an area of great interest reflects both the importance and the complexity of this topic." Admittedly, much research continues even after a century of progress.

Near-Field vs. Far-Field

At present, drag over a finite wing can be extracted from a numerical flow solution via two methods: surface pressure integration about the wing surface or a far-field analysis. The surface integration method, also called the "near-field method" is elementary by design and simply gives a mechanical breakdown of the forces acting on the wing into its normal component and its tangential component. Most all commercial CFD codes include this method as a tool for estimating drag.

Far-field analyses are performed in the wake region and thus are often referred to as wake integration techniques. This technique for determining drag, or in some cases lift, on a body is based on a control volume approach. Special care is taken so that the control volume is large enough so as to assume negligible flow escapes the control volume at any face other than the downstream outflow face. This ensures that all appreciable changes in the flow due to the body will be evident on this downstream face. A momentum balance is then applied over the inlet and outlet to calculate the drag force. The conservation equations are used to develop integral relations which can be performed over the rear outflow face to calculate the drag force. The wake integration method is commonly referred to as Trefftz plane integration; named after Trefftz, one of the first to use a far-field technique for determining induced drag in the early 1920's. The wake integration plane, or Trefftz plane, is placed aft of the wing as is orientated perpendicular to the freestream direction.

Nikfetrat et al. [8] used a far-field technique to evaluate drag in an Euler simulation. A wing with an elliptic spanwise chord distribution made of NACA 0012 airfoil sections and having an aspect ratio of seven was used. The far-field technique coupled with an Euler solution provides a decomposition of total drag into induced and wave drag, and thus provides more information on drag sources than that of surface pressure integration. The focus of the paper is to draw a comparison between the drag obtained from evaluation of the wake integral to the more conventional drag based on the integration of surface pressures. Two separate Euler codes are used in the study. The lift coefficient obtained from both surface pressure integration as well as evaluation of the wake integral agree very well with lifting line theory and serve as a consistency check of

the numerical solution. However, the surface pressure integration severely overestimates the induced drag coefficient by more than 40% in both simulations. Evaluation of the wake integral, on the other hand, is within 1% of the value predicted by lifting line. The authors note that lifting line theory is known to be quite accurate for this high aspect ratio un-swept configuration at incompressible conditions. The wake integration plane is placed immediately aft of the trailing edge, yet no discussion or reasoning is provided for this placement.

Hunt et al. [9] also speak to the inadequacy of using a surface integral technique to calculate drag over a wing. They note that although theoretically sound, in practice artificial smoothing acts to corrupt the results. They go on to say that the effects of artificial smoothing appear as entropy in the far field creating a mismatch of the surface integration and far-field integration results, although from a momentum balance approach these methods should be equivalent. Wong et al. [10] is referenced for showing that although the far-field crossflow plane integration for induced drag was not greatly affected, the drag predicted by surface integration increased significantly as the level of artificial smoothing was increased.

Smith [11] suggests, "There is a substantial amount of evidence that the accuracy of surface pressure integration is insufficient for a careful study of induced drag and therefore alternate techniques are required." He notes that in typical wing configurations, this inaccuracy is likely due to subtractive cancellation that is inherent in surface pressure integration.

Amant [12] suggests, "Another way to tackle the problem is to study the influence of the model on the surrounding fluid, rather than the effect of the fluid on the body

skin." This is exactly the approach taken by a far-field method. Not only does the far-field method offer the potential for accurate calculations, "but it also gives the opportunity to extract each component of drag: viscous drag, wave drag, and induced drag." In fact, this strength of the far-field method is the reason many researchers choose it over the more basic near-field method of surface pressure integration.

<u>Far-Field Drag Studies</u>

Eppler [13] gives a sufficient yet concise explanation of the evolution of a wake region behind a wing as follows; "the drag causes a wake behind the airfoil which becomes with increasing distance of the airfoil wider and shallower." Wider refers to the spanwise direction while shallower refers to the deviation from freestream values. In essence, the drag acts to slow the air just behind the wing which causes the deviation from freestream velocities to decrease in the downstream direction yet spread to cover a larger area. Eventually a downstream distance is theoretically reached where the deviation from freestream is negligible so that in the limit as downstream distance approaches infinity, deviations from freestream velocities will disappear. If a control volume is fit around the wing to encompass the entire wake region at these distances as described, a simple calculation of pressure drop times the cross-sectional area of the control volume perpendicular to the freestream direction will yield the drag force. However, a computational domain of this size is rare in most situations, and an alternative method must be used to calculate drag.

Giles et al. [14] give a theoretical development for calculating drag via wake-survey methods. They use a momentum balance approach to develop a system of

integrals that "reduces the task of force computation to the integration of various flow parameters in a crossflow plane downstream of a body." Drag is decomposed into entropy, enthalpy, and vorticity components that are directly related to standard wave and profile drag, engine power and efficiency, and induced drag, respectively. Comparisons are drawn between experimental and computational formulations of the drag integrals, and equivalence is derived.

Kusunose [15] focuses a study on wind tunnel experiments and the analytical aspects of the determination of drag acting on such a model. He notes that "the drag of a model located in a control volume can be calculated from the change in momentum in the direction of the undisturbed free stream flow." His work includes a detailed derivation of the drag integral which contains individual integrals for profile and induced drag, using just such an approach.

Cummings et al. [16] and Schmitt et al. [17] both observe from far-field analyses of numerical studies that the transverse kinetic energy, and thus the induced drag, decreases downstream of the wing at a much faster rate than reality dictates. According to the Euler theoretical model, it should remain constant downstream. This phenomenon is attributed to artificial, or numerical, dissipation which can be quite strong in the far-field where cells typically grow unavoidably coarse. Schmitt et al. argue that these spurious contributions to drag cannot be separated from physical production by surface force integration because spurious contributions are embedded within the pressure and shear stress distribution over the wing surface.

Destarac [18] presents theoretical and numerical aspects of drag extraction including a drag balance, for which he credits J. van der Vooren [19], and numerical

deviations such as spurious production and transformation of drag components. He then moves on to discuss specific applications and drag reduction techniques. Destarac argues that the near-field far-field drag balance "ensures exact balance of pressure drag plus friction drag (near-field) and viscous drag plus wave drag plus induced drag (far-field)." He also notes that although the spurious drag appears explicitly in the farfield breakdown, it is actually implicit in the near-field breakdown. This is yet another argument for the far-field method as "this error can by no means be corrected using the near-field approach only." In reference to the downstream decay of crossflow kinetic energy, and thus induced drag, Destarac states, "In computations, mainly because of the coarseness of the grid in the downstream far-field, numerical smoothing dominates over physical dissipation and causes the trailing vorticity to decay….. There is neither loss nor production of total drag, but a transfer of one form of drag to another."

Hunt et al. [9] use cutoff parameters, based on viscosity and entropy, to reduce the size of the crossflow plane in an effort to increase accuracy and decrease computational time. Hunt et al. show that the size of the bounding control volume, more specifically the downstream distance of the outflow plane, does not significantly affect the induced drag calculation. However, it is noted that the values of induced drag decrease downstream due to numerical dissipation converting crossflow kinetic energy into entropy. This decrease in induced drag is complimented by a corresponding increase in entropy drag. Due to this "interchange of vorticity for entropy that is caused by numerical dissipation as the vortex convects downstream," it is suggested that the best position for the crossflow plane is in the near field just aft of the wing so as to largely avoid this phenomenon.

Bourdin [3,6] takes a look at the wingtip and planform effects on lift induced drag in his studies. He uses strictly Euler solutions arguing that the mechanism for producing lift induced drag, the influence of the wing trailing vortex sheet on the wing itself, is a fundamentally inviscid mechanism. He also points out that lower fidelity methods (vortex lattice methods (VLM), panel methods, full potential codes) are computationally less expensive, but a major weakness lies in their wake modeling which require wake geometry to be specified or fitted as a boundary condition a priori. Alternatively, Euler solutions are capable of capturing the freely deforming wake shape. Bourdin also uses the far-field technique, as opposed to surface pressure integration, which admittedly requires "complex post-processing of the numerical flow solution," but in its defense does give "a phenomenological breakdown into physical components (lift induced drag, wave drag, and with Navier-Stokes equations, viscous drag)." Noting that CFD numerical schemes along with their meshes produce spurious drag sources, Bourdin views this ability to provide a phenomenological breakdown as the main asset of the far field technique.

Knowing that part of the lift induced drag is transformed into spurious viscous drag, and does so mostly in the area of the wing tip vortex, Bourdin notes that this is an irreversible phenomenon and thus can be computed by applying an integral formula for irreversible drag between the wing tip vortex and the wake interrogation plane. Using ONERA software, he shows results from a study of induced drag over an elliptical planform using a multi-block structured grid. He plots what he calls the apparent lift induced drag, the irreversible correction, and the corrected lift induced drag. The corrected lift induced drag is simply a summation of the previous two drag forms. The most significant result from this study is that once corrected by the addition of the

13

irreversible drag, the corrected lift induced drag calculation is nearly independent of downstream location. This downstream independence is crucial if induced drag is to be used in an automated optimization routine.

Amant [12] also uses the far-field approach in wind tunnel applications as well as CFD solutions to calculate and decompose drag. He utilizes both an Euler solver as well as a Navier-Stokes solver. Although there is some significant error when applied to the wind tunnel experiments, largely due to instrumentation difficulties, the induced drag results from the CFD solver are very satisfactory. Amant also makes use of the ONERA post-processing software to enable the separation and elimination of spurious drag sources. Again, this allows induced drag calculations that are nearly independent of downstream location. Amant ignores an axial velocity deficit term, resulting from the presence of the vortical sheet, from the induced drag integral; this is discussed in a later section in more detail. This is a common practice due to its relatively smaller contribution when compared to the terms related to the action of the viscous layers.

Stewart [13] develops a method for estimating the exergy utilization of a wing in a low subsonic, three-dimensional, viscous flow field using a RANS solver. Assuming steady flow, this essentially requires the estimation of entropy generation. He develops a far-field method to calculate drag by establishing a relation between drag and exergy destruction. Using his newly developed methodology, his results compare satisfactorily to experimental data and lifting line theory, while surpassing the traditional surface integration results. He notes that "mapping of entropy generation clearly details regions of irreversibility in the flow field," and thus enables the designer to locate, and possibly reduce, sources of drag.

Far-field analysis of the crossflow kinetic energy has been performed for a number of years, and has become essentially the standard practice for calculating induced drag. Although spurious contributions are noted more and more, relatively few papers to date actually address this issue with actual CFD results. While the standard wake integration techniques require simple post-processing that is available in many commercial software applications, the extraction of the spurious drag requires a more hands-on approach involving cell-by-cell calculations that require access to the flow solver code itself.

Numerical Uncertainty

Concerns about numerical uncertainty have been around since the early 20th century, around the time of L. F. Richardson. Detailed history of the progress of numerical uncertainty efforts are outlined by both Freitas et al. [21] and Roache [22]; some highlights of which are repeated here. The realization of modern computers provided a means for significant advancement in this area, and in fact the first conference to truly address numerical uncertainty to any real extent was the Stanford Olympics of 1968 [23], the primary objective of which was to "identify the fundamental predictive capabilities of early CFD codes and turbulence models, as they related to turbulent boundary layer flows" [21]. A major step was taken by the *American Society of Mechanical Engineers (ASME) Journal of Fluids Engineering* in 1986 when they released the first editorial policy statement making it clear that the journal would "not accept for publication any paper reporting the numerical solution of a fluids engineering problem that fails to address the task of systematic truncation error testing and accuracy estimation" [24]. Although such testing and estimation is worthwhile, the policy failed to

define a set procedure for performing such an analysis. Discussions continued through the mid 1990's when policies were adopted by both ASME and AIAA to help control numerical accuracy.

Freitas et al. [21] review the progress made by ASME to quantify numerical uncertainty. It is important to note that ASME's Fluids Engineering Division (FED) does not attempt to set a specific level of acceptable uncertainty, citing that "the factors that define an acceptable solution and uncertainty band are unique to each simulation study." Rather than push for this threshold condition, ASME's FED simply attempts "to lay the foundation for all CFD simulations to include as part of the reporting of the results, an assessment of the uncertainty band for the pertinent variables of the simulation." Freitas et al. also admit that there are several existing methods for calculating numerical uncertainty and make no attempt to require a specific method. However, they do outline a specific procedure for the uniform reporting of grid convergence developed by Patrick Roache and based on Richardson Extrapolation.

Roache proposed the use of a Grid Convergence Index (GCI) in 1994 [25]. He argues that it "provides an objective asymptotic approach to quantification of uncertainty of grid convergence." Roache acknowledges that systematic grid convergence studies are arguably the most common and most reliable technique for quantifying numerical uncertainty. He also notes that the reporting of such studies is terribly inconsistent and even confusing. With this in mind, the general purpose of the GCI is to provide a common platform on which to compare grid convergence results. "The basic idea is to approximately relate the results from any grid convergence test to the expected results from a grid doubling using a 2$^{\text{nd}}$-order method." The method is, as stated above, based

upon the theory of generalized Richardson Extrapolation, however, it is not required that Richardson Extrapolation actually be used to improve the accuracy. A final redeeming quality for GCI is that it may easily "be applied *a posteriori* by editors and reviewers, even if authors are reluctant to do so." This is important not only when the author is reluctant, but also when reviewing papers written before such a process has become standard practice.

CHAPTER 3

OBJECTIVES

The primary objective of this thesis work is to develop a methodology for the extraction of accurate and robust estimates of induced drag from flow over a finite wing in a computational fluid dynamics (CFD) solution. To meet this objective, a computational domain will be created to surround a simple rectangular wing, which will be subjected to subsonic, inviscid, numerical simulation. The standard farfield technique will be amended in an effort to combat physical and numerical issues that arise. Modeling these issues to remove their influence will enable the extraction of an induced drag that more closely agrees with real-world physics and is truly independent of downstream location.

A second objective is to develop a methodology to extract, from CFD results, the spanwise lift distribution of an untwisted, finite rectangular wing. The resulting spanwise lift distribution will be compared against theoretical lifting line results for verification of the methodology. The lift distribution will also be compared against the distribution obtained by the pioneering work of Kolonay and Eastep [2] for further verification.

A third objective is to perform an initial uncertainty analysis on the prediction of induced drag. The performance of such an analysis on CFD data is still in its relative infancy, but will serve to provide a basic understanding of the benefits that can result from further uncertainty analyses.

CHAPTER 4

Model Development

Geometry and Flow Conditions

Two geometric configurations were studied in this investigation; a wing with a
NACA 0006 profile, and a wing with the NACA 0012 airfoil shape. Both wings were
symmetrical, untwisted rectangular planform with aspect ratios of 6.67. The wing with
the NACA 0012 cross-section is presented in Figure 1. The total wingspan is forty feet
(half-span of twenty feet) and the chord length is six feet. Most work was conducted at a
freestream mach number of 0.3, however the velocity was varied in the subsonic and
transonic flight regimes to gain an understanding of the affects. The geometric angle of
attack was set at five degrees to avoid the complications of high angles of attack, namely
flow separation, while still providing sufficient lift for accurate calculations. The study
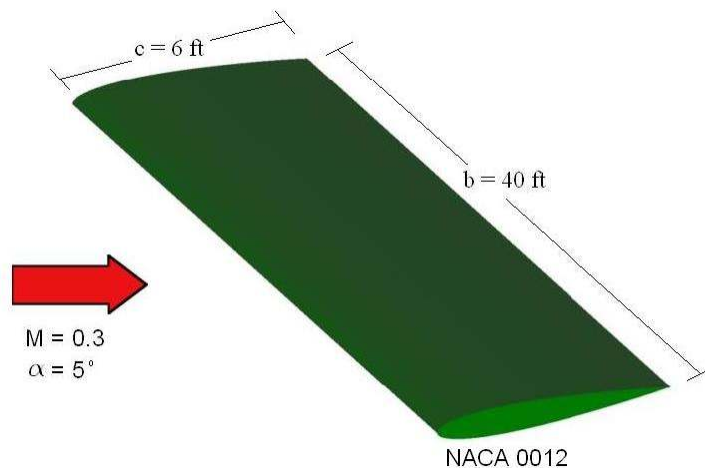was also restricted to steady, level flight at sea level conditions.

Figure 1. Wing Geometry

The domain of interest for this study consisted of uniform flow past a three-dimensional wing. Due to the assumption of symmetrical wing loading and wing geometry about the span for level flight, the modeled domain includes only half of the wing with one domain boundary designated as the plane of symmetry. This approach will roughly halve the computational expense by allowing the computational domain, and therefore the number of total cells, to be cut in half.

With the wing geometry and flow conditions determined, grid construction followed a systematic process. Points were imported from a NACA four-digit series profile generator to form the wing's airfoil cross-section. These points were connected utilizing a polynomial curve fit to form three individual panels; the lower surface, the upper surface, and the control surface. Together, these three panels form a complete cross-sectional loop. The airfoil section was rotated five degrees to generate the proper angle of attack, and the wing surface itself was then extruded from this 2D airfoil shape into twenty equal spanwise segments to allow for later spanwise calculations. A representation of these extruded surfaces can be seen in Figure 2.
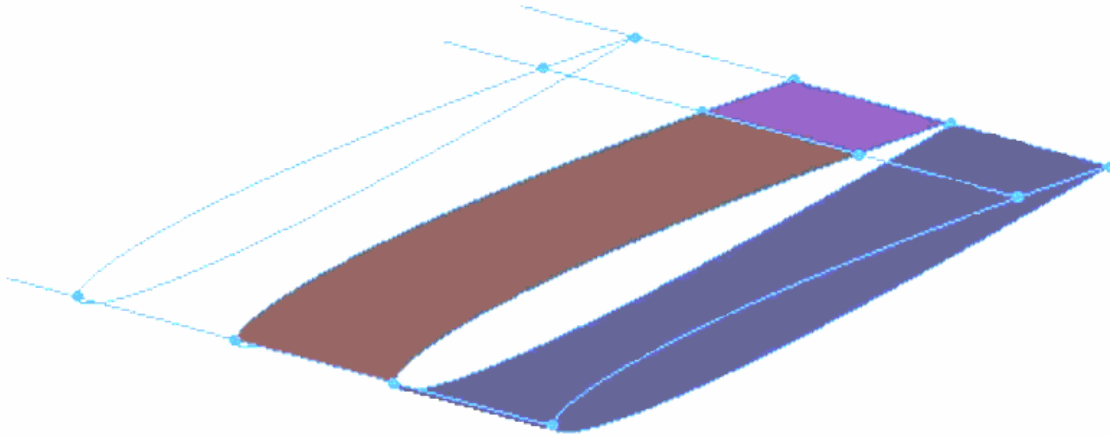
Figure 2. Wing panel construction

A second surface is wrapped around the wing to form a far-field boundary condition, as seen in Figure 3, at a minimum of five chord lengths spacing from the wing surface in any given direction and extending far enough downstream to capture all necessary wake effects. The far-field surface follows a curve along the upstream side of the wing in order to minimize the number of cells, and therefore computation cost.

Once the wing geometry and control volume are outlined, an unstructured mesh is generated on all surfaces; including wing panels and far-field surfaces. The grid generation software then fills in the three-dimensional control volume itself with unstructured cells based upon the user designated grid points. An unstructured mesh was chosen to ensure the minimum number of cells, as compared to a structured Cartesian mesh, as well as to easily interface with the given flow solver. Also, since an unstructured cell does not require opposing sides to have the same number of grid points, cells may be clustered in the vicinity of solid surfaces and grow relatively coarse where freestream conditions are expected.

A couple of methods were used in order to minimize the number of total cells while still enhancing the accuracy of the solution. As shown in Figure 3, a permeable surface was constructed along the anticipated wake plane in order to ensure clustering of grid points in the wake region of the flow. Clustering was also used along the leading and trailing edges of the wing, the region just aft of the trailing edge where the wake begins, and the virtual control surfaces found along the trailing edge of the wing. Much of this clustering can be seen in Figure 4. Again, the use of unstructured cells allows the

abovementioned clustering of grid points in regions of interest, but then grid relaxation to

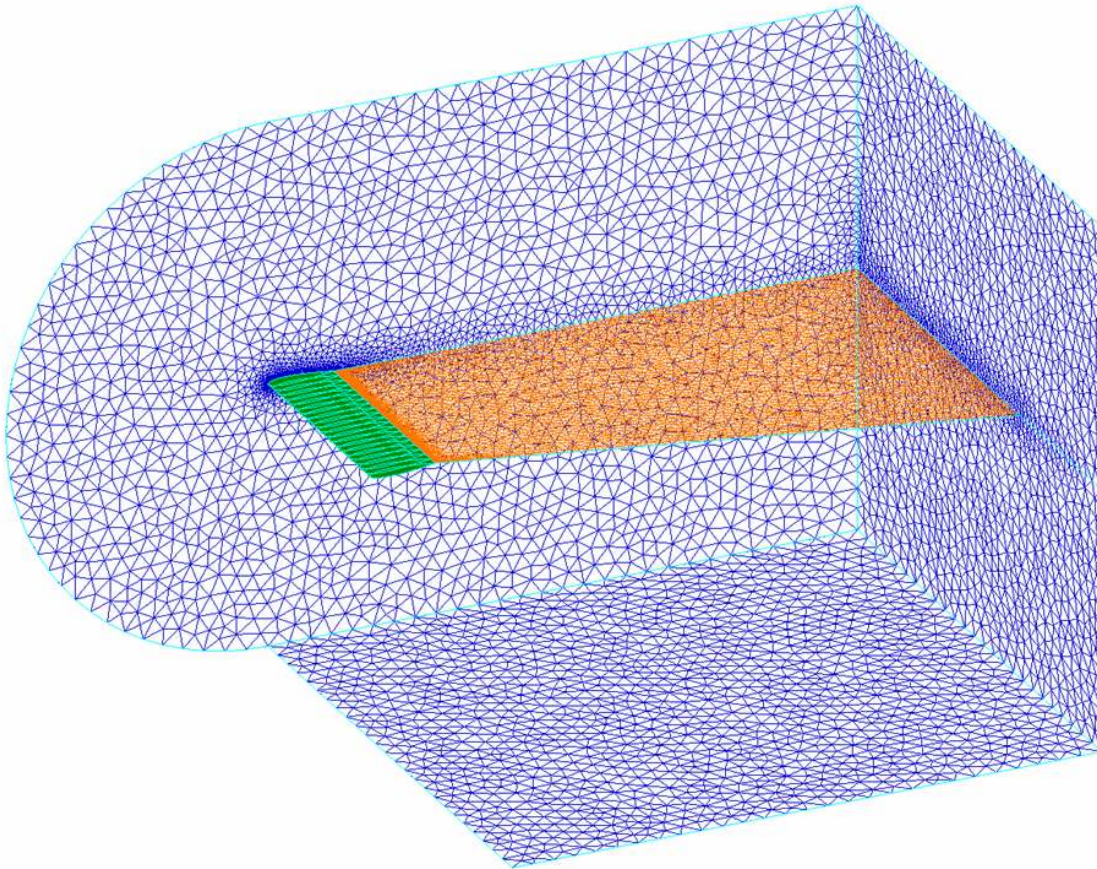a relatively coarse mesh towards the far-field boundary.

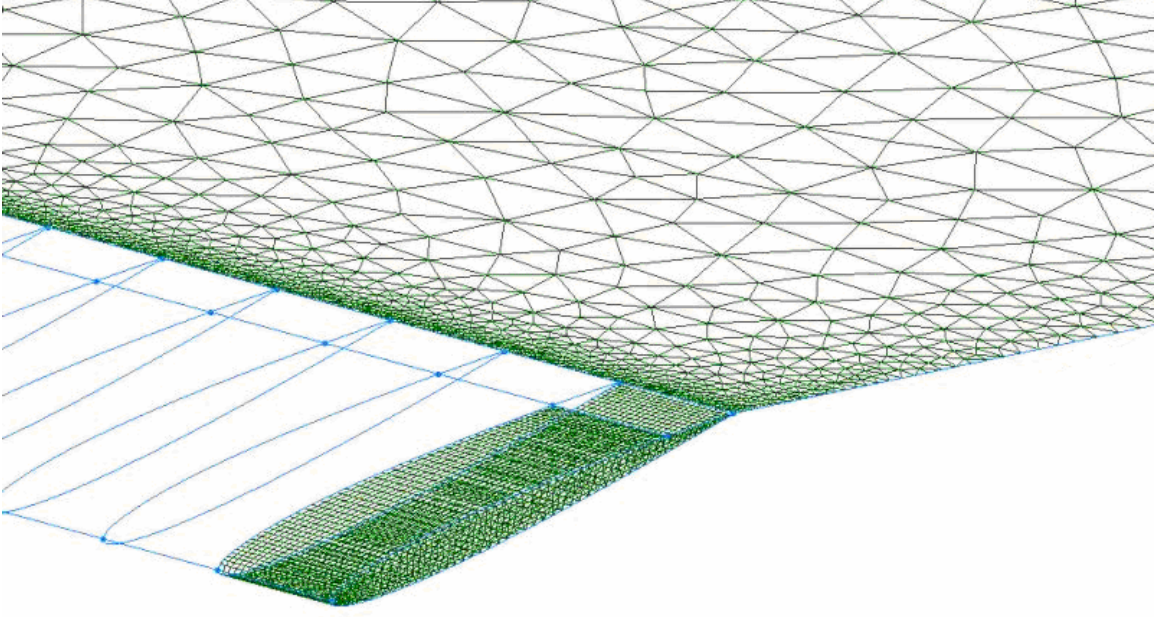**Figure 3: Permeable wake plane surface and far-field boundaries**

Figure 4. Clustering of unstructured mesh

Flow Solver

AVUS (Air Vehicles Unstructured Solver) was utilized as the flow solver for this thesis research. AVUS, formerly Cobalt$_{60}$, is an in-house research code maintained by the US Air Force Research Lab's Air Vehicles Directorate – Computational Sciences branch. AVUS is designed primarily for unstructured grids, but structured grids may be used if a mesh's structure is defined explicitly. AVUS is capable of handling two or three dimensions, as well as axis-symmetric grids. Viscous fluxes have the option of being neglected in order to process inviscid flows. AVUS solves the Euler and Navier-Stokes equations in an inertial reference frame and, in integral form, the Navier-Stokes equations are [21]:

$$\frac{\partial}{\partial t}\iiint_{\forall} Q dV + \iint_{\delta} \left(f\hat{i} + g\hat{j} + h\hat{k}\right)\cdot\hat{n}dS = \iint_{S}\left(r\hat{i} + s\hat{j} + t\hat{k}\right)\cdot\hat{n}dS . \tag{1}$$

where:

25

$$Q = \begin{bmatrix} \rho \\ \rho u \\ \rho v \\ \rho w \\ \rho e \end{bmatrix} \qquad f = \begin{bmatrix} \rho u \\ \rho u^2 + p \\ \rho uv \\ \rho uw \\ u(\rho e + p) \end{bmatrix}$$

$$g = \begin{bmatrix} \rho v \\ \rho uv \\ \rho v^2 + p \\ \rho vw \\ v(\rho e + p) \end{bmatrix} \qquad h = \begin{bmatrix} \rho w \\ \rho uw \\ \rho vw \\ \rho w^2 + p \\ w(\rho e + p) \end{bmatrix} \qquad (2)$$

and

$$r = \begin{bmatrix} 0 \\ \tau_{xx} \\ \tau_{xy} \\ \tau_{xz} \\ a \end{bmatrix} \qquad s = \begin{bmatrix} 0 \\ \tau_{xy} \\ \tau_{yy} \\ \tau_{yz} \\ b \end{bmatrix} \qquad t = \begin{bmatrix} 0 \\ \tau_{xz} \\ \tau_{yz} \\ \tau_{zz} \\ c \end{bmatrix}. \qquad (3)$$

In this case $a = u\tau_{xx} + v\tau_{xy} + w\tau_{xz} + kT_x$, $b = u\tau_{xy} + v\tau_{yy} + w\tau_{yz} + kT_y$, and $c = u\tau_{xz} + v\tau_{yz} + w\tau_{zz} + kT_z$; V is the fluid element volume; S is the fluid element surface area; $\hat{n}$ is the outward-pointing unit normal to S; $\hat{i}$, $\hat{j}$, and $\hat{k}$ are the Cartesian unit vectors; ρ is the density; p is the pressure; u, v, and w are the velocity components; e is the specific energy per unit volume; T is the temperature; k is the thermal conductivity; and τ_{xx}, τ_{yy}, τ_{zz}, τ_{xy}, τ_{xz}, and τ_{yz} are the viscous stress tensor components. This system of equations is closed by the ideal gas law and nondimensionalized by freestream density and speed of sound.

AVUS is based upon a first-order accurate, exact Riemann method developed by Gottlieb and Groth [27]. Second-order spatial and temporal accuracies, as well as implicit time stepping, are built upon this core procedure. AVUS uses a cell-centered, finite volume approach.

CHAPTER 5

ANALYSIS

Lifting Line Theory

Thin airfoil theory provides a method to calculate the lift of a two-dimensional airfoil. A substantial assumption in the theory requires that the span of these airfoils is infinite, which in turn produces a constant lift distribution along the infinite span. Finite wings differ, of course, in that they have a finite span. As the high-pressure flow on the underside of the wing tends to flow outward towards the tip and the low-pressure flow above the wing tends to flow inward towards the root, a trailing vortex is formed as these two flows meet at the trailing edge. Figure 5 clearly shows this vortex as it forms aft of the wing.

Wake Vortex Study at Wallops Island
NASA Langley Research Center   5/4/1990   Image # EL-1996-00130

Figure 5. Wing tip vortex

This trailing vortex sheet and the tendency for these pressures to equalize induces a downwash velocity, visible in Figure 6, in the downward direction, normal to the undisturbed free stream, defined as

$$w(z) = -\frac{1}{4\pi} \int_{-b/2}^{b/2} \frac{\Gamma'(z)}{z_0 - z} dz \qquad \textbf{(4)}$$

where $\Gamma(z)$ represents the span-wise circulation distribution and b is the total span length. This downwash velocity alters the approach angle of the free stream flow by an amount termed the downwash angle defined as

$$\in (z) = \tan^{-1} \frac{w(z)}{U_\infty} \qquad \textbf{(5)}$$

D_v, induced drag

Lift

Effective lift, acts normal to the effective flow direction

Chord line

α_e

α

ϵ

U_∞

ϵ

w

Undisturbed free-stream direction (direction of U_∞)

The resultant velocity for airfoil-section

—·— Chord-line of the airfoil

——— Effective flow direction

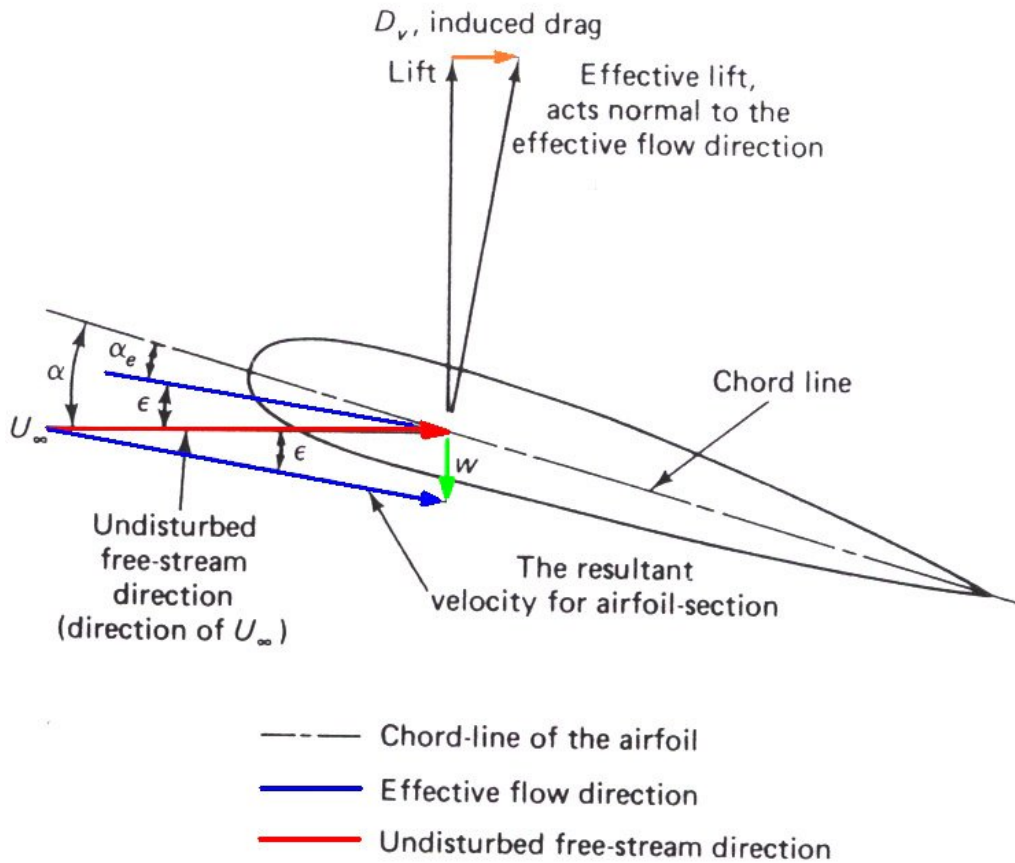——— Undisturbed free-stream direction

Figure 6. Induced flow over airfoil

which is often simplified to

$$\in(z) = \frac{w(z)}{U_\infty} \tag{6}$$

where U_∞ represents the undisturbed freestream velocity. The effective angle of attack at a given span-wise location then is defined as

$$\alpha_e(z) = \alpha - \in(z) \tag{7}$$

where a represents the geometric angle of attack. The downwash velocity increases along the span from root to tip, resulting in a span-wise lift distribution that drops as you approach the wingtip. It is also important to note that since lift acts normal to the freestream velocity direction, the effective lift will act normal to the effective freestream velocity as shown in Figure 6. It follows, then, that the effective lift has also been altered by the same downwash angle. This effective lift has a force component in the direction of the undisturbed freestream velocity which is termed lift induced drag; the focus of this project.

Glauert considered a circulation distribution expressed by a Fourier sine series, the first term of which represents the elliptic distribution. A circulation distribution then can be defined as

$$\Gamma(\phi) = 4sU_\infty \sum_1^N A_n \sin(n\phi). \tag{8}$$

where s represents the half-span length and the number of terms, N, is determined by the desired number of discrete span-wise locations used to describe the distribution. The physical span-wise coordinate has been replaced by ϕ according to the transformation:

$$\frac{z}{s} = -\cos\phi .\tag{9}$$

Since the span-wise lift distribution represented by the circulation is symmetrical, only the odd terms are used. A derivation is given by Bertin and Smith [28] that concludes with the governing equation shown here, termed the *monoplane equation*;

$$\mu(\alpha - \alpha_{0l})\sin\phi = \sum_{1}^{N} A_n \sin(n\phi)(\mu n + \sin\phi).\tag{10}$$

where μ is defined as

$$\mu = \frac{ca_e}{4b} .\tag{11}$$

and a_e, the lift curve slope, is assumed to be 2π according to thin airfoil theory. After solving for the Fourier coefficients, lift and drag characteristics can be calculated. The total lift coefficient can be approximated using the equation

$$C_L = A_1\pi \cdot AR\tag{12}$$

where C_L is dependent only on the first Fourier coefficient, regardless of the number of terms in the series. The coefficient of induced drag can also be approximated by

$$C_{Di} = \frac{C_L{}^2}{\pi \cdot AR}\left[1 + \left(\frac{3A_3{}^2}{A_1{}^2} + \frac{5A_5{}^2}{A_1{}^2} + \frac{7A_7{}^2}{A_1{}^2} + \cdots + \frac{nA_n{}^2}{A_1{}^2}\right)\right]\tag{13}$$

which is obviously influenced by the number of terms used. As more terms are added to the Fourier sine series, the induced drag coefficient will more nearly approximate the asymptotic value. The span-wise lift coefficients can also be approximated for a given span-wise unit section by

$$C_l(\phi) = \frac{\rho_\infty U_\infty \Gamma(\phi)}{\frac{1}{2}\rho_\infty U_\infty{}^2 c} = \frac{2\Gamma(\phi)}{U_\infty c} .\tag{14}$$

It is also important to account for compressibility effects, which can be easily done by applying the Prandtl-Glauert Formula [28]; defined as

$$C_p = \frac{C'_p}{\sqrt{1 - M_\infty{}^2}}.$$

(15)

At low Mach numbers, just as you would expect, this will not have much affect on the outcome of the calculations. However, at higher Mach numbers the effects become very noticeable. Figure 7 shows the results on the span-wise lift distribution with and without the discussed compressibility effects at differing Mach numbers. At a Mach number of 0.3, compressibility effects alter the lift distribution by about 5%, whereas at a Mach number of 0.7 the effect is closer to 40%.
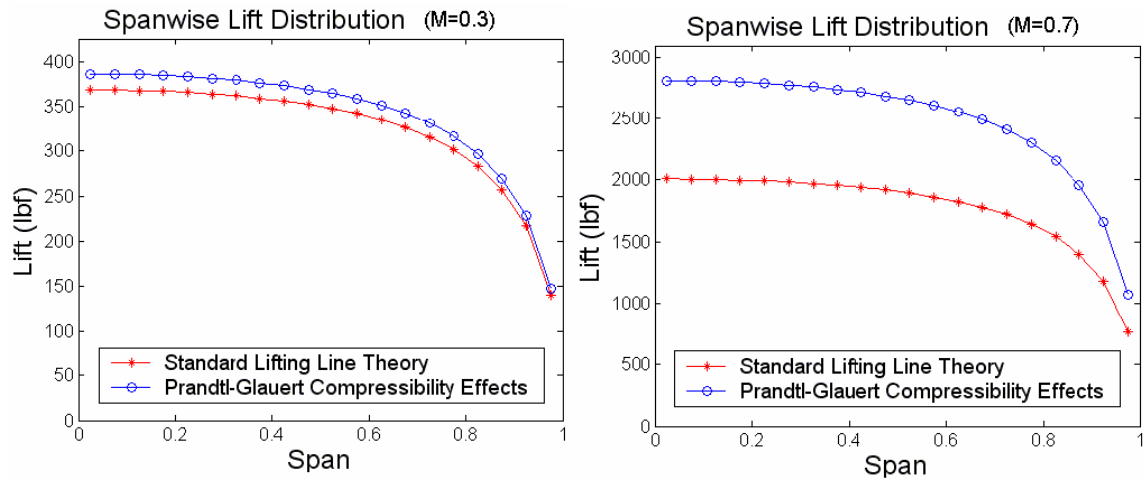

Figure 7. Compressibility effects

With efficiency in mind, a lifting line code was written by the author using MATLAB to automate the theoretical calculations. Given a set of geometric and flow condition inputs, the code returns a multitude of output variables as displayed in Figure 8. Each of these variables is available for manipulation and/or plotting upon completion of the code. Care was taken to write the code in general terms to ensure flexibility across

varying input conditions. The code also has the ability to read in post-processed results from numerical cases in order to compare, as well as report the error, when fitting the numerical results over the theoretical. A sample output from the code can be seen in Figure 9.
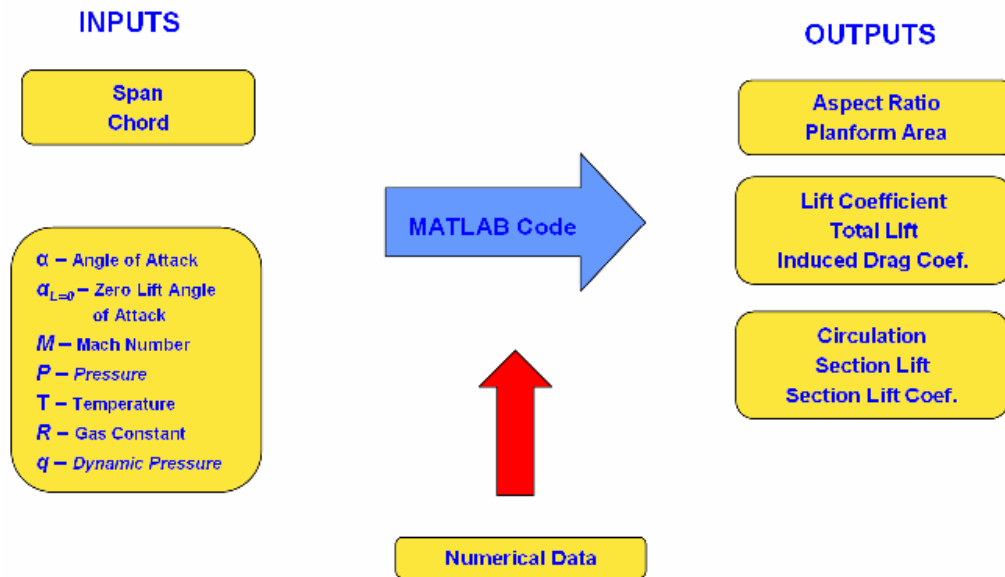

Figure 8. Lifting Line code – Inputs/Outputs

Figure 9. Example output screen from MATLAB code

Induced Drag Calculation

In computational fluid dynamics, we have generally two methods for calculating the lift-induced drag of a wing, a surface integration method and a wake integration method. As discussed in a previous section, this work utilizes the wake integration approach. The surface integration method relies on calculations of pressure and skin friction over a series of flat surfaces (facets) that approximate curved surfaces of a three-dimensional wing. The sensitivity of computing aerodynamic drag using a surface integration method can lead to a notable uncertainty, although it is suitable for computing the lift force coefficient computations because lift tends to be one or two orders of magnitude larger than drag force coefficients. For accurate, robust drag calculation, the far-field volume-integral or wake-integration (Trefftz-plane) approach appears to be a worthwhile alternative and one that allows the drag to be estimated by its components, namely profile, wave, and induced drag [3,14,19].

The wake integration method, also often referred to as Trefftz-plane analysis, quantifies induced drag by extracting flow data from a cut-plane downstream of the wing and perpendicular to the freestream direction. This analysis often takes place in post-processing since it requires interpolating flow field data to arbitrary planes where the nodes or cell centers of a CFD grid do not necessarily intersect. The Trefftz-plane integration equation is derived from the momentum equation of the governing equations of fluid mechanics.

Assuming steady state flow and negligible body forces, the drag of a wing in a CFD model can be found from a momentum balance on the wing of Figure 10 as

$$D = \int_{S_1} \left(P_\infty + \rho_\infty U_\infty^2 \right) dydz - \int_{S_2} \left(P + \rho u^2 \right) dydz \tag{16}$$
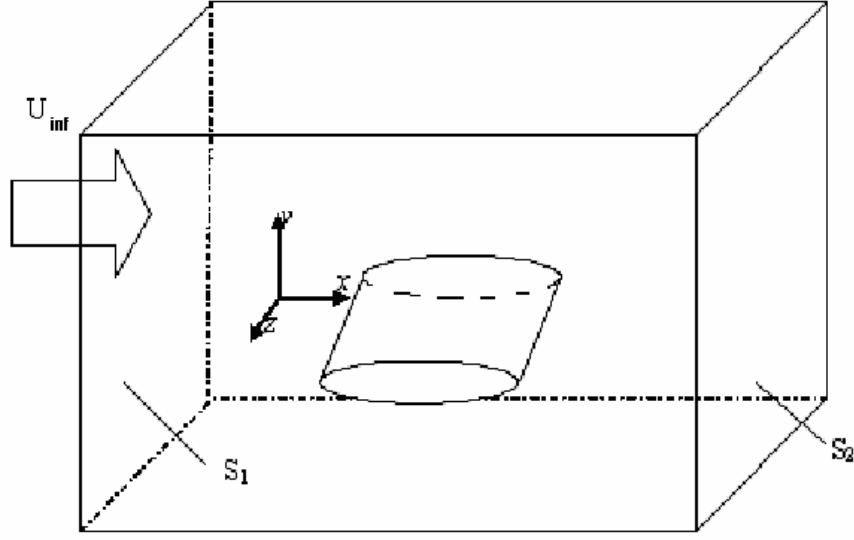
Figure 10. Schematic representation of control volume around a finite wing

In Figure 10, S_1 and S_2 represent the traverse planes located upstream and downstream respectively of the wing. The first and second terms on the right hand side of the equation represent the pressure forces driving the flow through the control volume and the flux of momentum across the faces of the control volume. Conservation of mass for steady flow through the control volume is given as

$$0 = \oint_S \rho \left(\vec{u} \cdot \vec{n} \right) dS .$$ **(17)**

Assuming the upstream and downstream planes have equivalent areas, the drag equation is rewritten as

$$D = \int_{S_2} \left[\rho u (U_\infty - u) + (P_\infty - P) \right] dy dz$$ **(18)**

In a manner presented by Kusunose [15], small perturbations are assumed in the properties of the downstream flow so that further substitutions and simplification gives

$$D = \int_{S_2} \left(\rho_\infty U_\infty (U_\infty - u) + (P_\infty - P) - \rho_\infty \left(1 - M_\infty^2 \right) \Delta u^2 + O(\Delta u)^3 \right) dy dz$$ **(19)**

In order to put this equation in terms of entropy production, an enthalpy change is introduced,

$$D = \int_{S_2} \left(\begin{array}{c} \rho_\infty U_\infty (U_\infty - u) + (P_\infty - P) - \rho_\infty (1 - M_\infty^2) \Delta u^2 + \rho_\infty (h - h_\infty) \\ - \rho_\infty (h - h_\infty) + O(\Delta u)^3 \end{array} \right) dydz \qquad (20)$$

where the enthalpy change is given as

$$h - h_\infty = U_\infty (U_\infty - u) - \frac{v^2 + w^2}{2} - \frac{\Delta u^2}{2} \qquad (21)$$

and substituting back, we obtain

$$D = \int_{S_2} [\rho_\infty (h - h_\infty) - (P - P_\infty) + \rho_\infty \frac{v^2 + w^2}{2} - \rho_\infty \frac{(1 - M_\infty^2)}{2} \Delta u^2 + O(\Delta u)^3] dydz . \qquad (22)$$

The second law of thermodynamics and Gibbs' equation give the connection between enthalpy and entropy, which when substituted gives

$$D = \int_{S_2} [\frac{P_\infty}{R} (s - s_\infty) + \rho_\infty \frac{v^2 + w^2}{2} - \rho_\infty \frac{(1 - M_\infty^2)}{2} \Delta u^2 + O(\Delta u)^3] dydz . \qquad (23)$$

This expression can be decomposed into two drag contributions: the induced drag and the profile drag. The induced drag is given by

$$D_i = \int_{S_2} \left(\rho_\infty \frac{v^2 + w^2}{2} \right) dydz \qquad (24)$$

The profile drag is represented by

$$D_p = \int_{S_2} \left(\frac{P_\infty}{R} (s - s_\infty) \right) dydz \qquad (25)$$

The remaining terms of Equation (23) represent higher-order terms and are consequently

ignored in many classical Trefftz plane analyses [14, 19, 29].

CHAPTER 6

RESULTS

Spanwise Lift Distribution

The span-wise lift distribution of the wing was generated to compare numerical data with lifting line theory. The computation of span-wise lift distribution like with the calculation of induced drag was computed as a post-processing step. In this computation, a wing was divided into sections. Each section was split at the chord line dividing the sections into their upper and lower surfaces. The static pressure was integrated over the section surfaces to generate the axial and normal components of force over each section.

$$N = \int_{LE}^{TE} p_l b \cos\theta dx - \int_{LE}^{TE} p_u b \cos\theta dx \qquad (26)$$

$$A = \int_{LE}^{TE} p_l b \sin\theta dx - \int_{LE}^{TE} p_u b \sin\theta dx \qquad (27)$$

The normal and axial forces in addition to geometric angle of attack were then used to calculate the average lift of each wing section [2].

$$L = N \cos\alpha - A \sin\alpha \qquad (28)$$

Figure 11 gives a visual representation of the rectangular wing span-wise lift distribution. The lift is plotted in the half span from wing root to wing tip, and the elliptical lift distribution plotted is presented strictly for comparison.
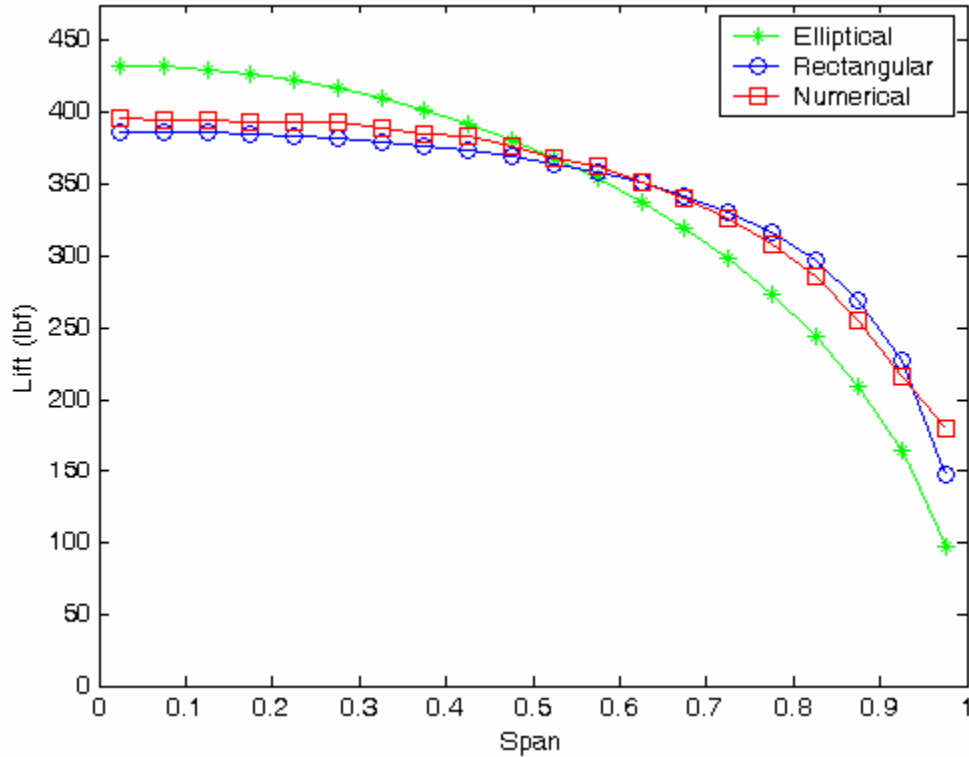
Figure 11. Span-wise lift distribution of a rectangular wing

The results from the span-wise lift analysis show that the numerical results correlate well with those of lifting line theory. The agreement between the two is within 2.4%. A large part of this error can be attributed to tip effects where the flows from the upper and lower surfaces of the wing interact. Rounding of the wing tip would most likely improve agreement.

<u>Induced Drag</u>

The results from the Trefftz-plane analysis contain much detail. Several numerical experiments were performed to study the effects of domain size and grid refinement on the predicted drag. Figure 12 shows the lift-induced drag coefficient results for multiple grids of varying size. The lift-induced drag coefficient results are shown normalized by the theoretical value obtained from lifting line theory. Each line in the figure represents a
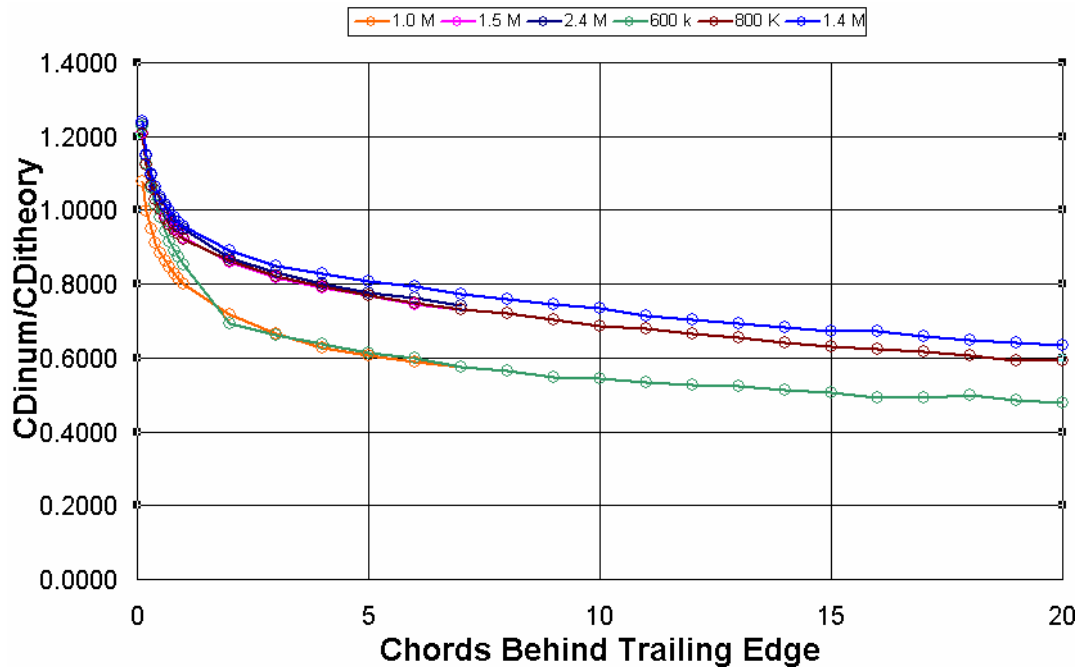
Figure 12. Induced Drag - Trefftz plane analysis of various grids at Mach 0.3

single grid, and the information in the legend indicates the size of each mesh represented. For example, the 1.0M line indicates that the grid contains one million cells. The grids portrayed in the figure are also characterized by different attributes. Some grids encompass a large domain focus while others span smaller domains (from the trailing edge of the wing in the streamwise direction). The grids with a larger domain extended much further downstream as well as several chord lengths further away from the wing geometry in the spanwise direction. The grids with a smaller domain had the far-field surface located only several chord lengths downstream from the wing's trailing edge.

In Figure 12, three grids map only to seven chord lengths behind the wing's trailing edge because those grids possessed a small domain focus. Testing grids with large and small domain focus allowed for verification of the far-field boundary condition. The circles that cover the lines indicate different Trefftz-plane surveys taken downstream

39

of the wing. The different plots show that a grids outer boundary distance from the wing geometry does not significantly influence the induced drag calculations. This demonstrates that the wing can be modeled with a relatively smaller domain without polluting the solution from the far-field boundaries. The observed trend from the data indicates that as the grid density increases the numerical results approach the value predicted by lifting-line theory.

Another and perhaps more obvious trend can be observed: the induced drag decreases as Trefftz-plane analyses progresses further downstream of the wing. Ideally the induced drag calculation should be independent of the downstream location of the Trefftz-plane. Several factors likely contribute to this phenomenon. One is a near-field effect. Ideally, the Trefftz-plane is located far downstream (infinity) such that longitudinal velocity components have diminished. The second is due to higher order terms in Equation 23. Lastly, the continued gradual decrease in (numerical) lift-induced drag with downstream location observed in Figure 12 is the result of spurious drag contributions, which act to dissipate the strength of the wing tip vortex and, consequently, the induced drag. Spurious drag is an artificial phenomenon attributed to the relaxation of the grid cells downstream of the wing and the effect of artificial (numerical) viscosity. Grid cell relaxation (or grid stretching) is used to improve computation times by using larger cells away from regions of significant flow activity, like the lifting wing geometry, thereby reducing the total cell count in a grid. This is a good trait for a CFD grid when considering analysis completion times and results convergence. However, this attribute is also a negative because it contributes to the error brought on by artificial viscosity. Artificial viscosity is the component of spurious drag that is associated with the

formation of the convective fluxes in an inviscid flow solver. Inviscid flow by definition contains no dissipative effects and therefore has no viscosity; however, the fluid flow solver creates numerical dissipation when the convective fluxes are discretized. Also, numerical damping, which again adds dissipation, can be used to improve steady-state convergence. To correct these errors, different formulations were investigated to improve results.

Van der Vooren and Slooff [19] used a near-field "correction" to the Trefftz-plane analysis that includes the second-order term (Equation 23) originally neglected in the classical Trefftz-plane lift-induced drag formulation,

$$D_i = \frac{1}{2}\rho_\infty \iint\limits_{S} \left[(v^2 + w^2) - \left(1 - M_\infty^2\right)\Delta u^2 \right] dA \tag{29}$$

Figure 13 presents two grids utilizing this near field correction. The plot shows both the classical Trefftz-plane as well as near-field corrected (denoted 'B') results for both grids.
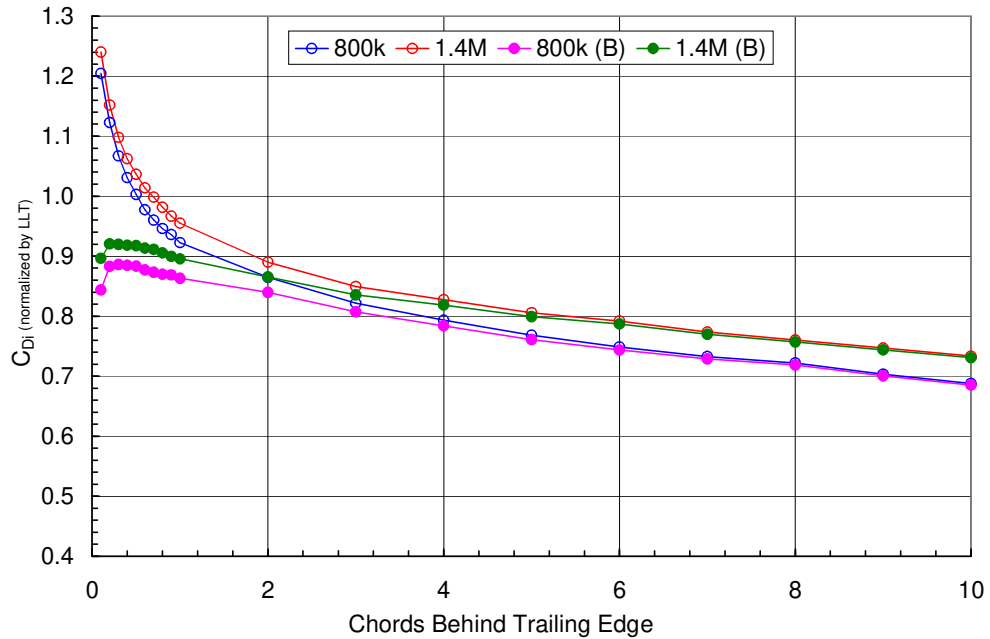

Figure 13. Near field correction of the Trefftz-plane results

41

With this correction, the overall induced drag prediction is improved within the first few chord lengths of the wing. This result is expected since the classical Trefftz-plane analysis is built on the assumption that the axial velocity is no longer changing. Similarly, note that beyond two or three chord lengths downstream of the wing, where the change in axial velocity is negligible, the near-field correction no longer deviates from the traditional Trefftz-plane results. Also note that the results of the two grids differ because one mesh was finer compared to the other, as indicated in the legend. The finer mesh was designed to have a higher grid cell density in the wing near-field wake region. The correction still retains some systematic error in the far field as evidenced by the location dependent value of induced drag. To correct for this error, Bourdin [6] and Van der Vooren et al. [19] suggest applying a volume integral correction for the irreversibilities brought on by artificial viscosity from the origin of the wing tip vortex to the Trefftz plane. This "irreversible correction" is currently under study, although it is not applied here.

<u>Uncertainty Analysis</u>

For a prediction to be useful in design it needs to be validated and its errors quantified. Numbers assigned to errors are called uncertainties. Here, an initial uncertainty analysis is applied to the prediction of induced drag. Ultimately, the uncertainty in question can be estimated by the root-sum-square of the individual contributing uncertainties as [20]

$$U = \sqrt{\sum_{k=1}^{K} U_k^2} \qquad (30)$$

assuming that (1) each uncertainty can be decomposed into a random uncertainty and a systematic uncertainty, (2) each uncertainty is evaluated at the same confidence level, and (3) the systematic errors identified are uncorrelated. Random errors are those errors that contribute to data scatter, whereas systematic errors contribute to a bias or offset of the data from its true value. An attempt is made to estimate uncertainties at a 95% confidence level.

The studies of this problem within our lab shows that our computational domain is sufficiently large to minimize the effects of far-field boundary conditions to under 1%, so we assign $U_{domain}/C_{Di} = \pm 1\%$. The finest grid studies using surface integral integration to estimate induced drag can do no better than $\pm 4\%$ of the lifting line prediction. We do not know the correct value for induced drag given the assumptions inherent in the lifting line theory that do not hold for a full flow field solution, which we presume will decrease the induced drag value a small amount [3], so we assign an uncertainty in our reference value of $U_{ref}/C_{Di} = \pm 5\%$.

A grid convergence index (GCI) study was completed to provide an estimate of the magnitude of discretization and convergence errors. The GCI for the finest grid is shown by Roache [22] to be

$$GCI_{fine} = F_S |E_1| = F_S \frac{|\varepsilon|}{r^p - 1} \tag{31}$$

where r is the grid refinement ratio, p is the order of convergence, F_S is the factor of safety, and E_1 is the error estimate from generalized Richardson Extrapolation (RE). The value of the error is found from

$$\varepsilon = \frac{f_2 - f_1}{f_1} \qquad\qquad (32)$$

where f denotes the parameter of interest, in this case induced drag, and the subscript 1 refers to the finest grid used. Experience [22] suggests that the accepted value of $F_S = 1.25$ be used for three or more grid refinement studies but $F_S = 3$ be used for two grid refinement studies to achieve conservative estimates at the uncertainty equivalent of 95% confidence. Adopting this to the methodology well used for reporting experimental uncertainty [20], we write

$$U_{GCI} = \pm GCI \qquad (95\%) \qquad\qquad (33)$$

Figure 14 shows that the relative uncertainty in induced drag due simply to the grid convergence, U_{GCI}/C_{Di}, ranged from 5% at a single chord length downstream to as much as 10% at 10 chord lengths downstream with 95% confidence. The values in the legend correspond to the number of cells in the coarse and fine grids, respectively.
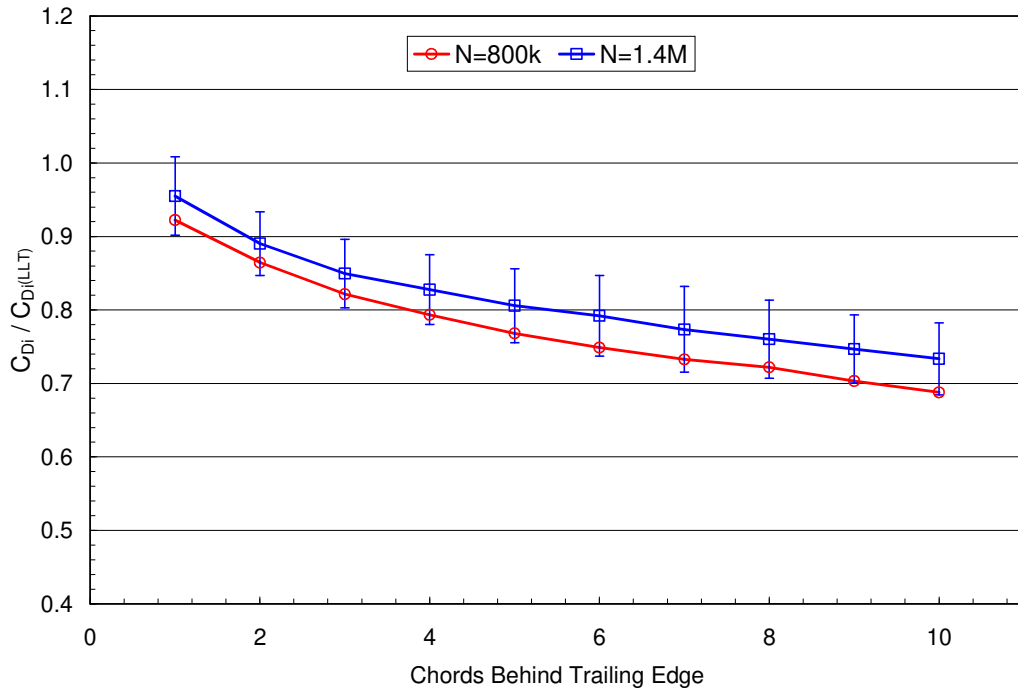

Figure 14. Grid Convergence Index (GCI) Study

We must also account for the dissipation downstream due to artificial viscosity. This will be treated as a non-symmetric systematic uncertainty since the artificial viscosity will always act to decrease the induced drag estimate. To estimate the potential magnitude of this uncertainty, we use lifting-line theory as our reference value. We have previously accounted for the uncertainty in the lifting-line prediction as U_{ref}, but the effect of artificial viscosity is a non-symmetric uncertainty, U_{diss}/C_{Di} . This uncertainty contribution is calculated as laid out by ASME PTC 19.1 Section 8.2.1 [30]. We believe that the true value falls between the numerical prediction and the value provided by our reference, lifting-line theory. In this we assume our lower level $B^- = 0$. If we made a correction to account for the effect of artificial viscosity, we would set B^+ equal to the uncertainty in that correction. But we do not make that correction. Instead, we set B^+ equal to the deviation between the numerical and lifting line prediction at each chord-wise location. This approach contributes a large uncertainty to our solution, as it should given the effect the chordwise location has on the predicted induced drag. Accordingly, we have identified 4 errors to which we need to assign uncertainties so that

$$\frac{U_{C_{Di}}}{C_{Di}} = \sqrt{\left(\frac{U_{domain}}{C_{Di}}\right)^2 + \left(\frac{U_{ref}}{C_{Di}}\right)^2 + \left(\frac{U_{GCI}}{C_{Di}}\right)^2 + \left(\frac{U_{diss}}{C_{Di}}\right)^2} \tag{34}$$

The resulting uncertainty is plotted in the form of traditional 'error bars' along the plot of the fine mesh grid as seen in Figure 15. The uncertainty in C_{Di} varies from $0.83 < C_{Di} < 1.12$ just downstream of the wing to $0.64 < C_{Di} < 1.09$ at 10 chord lengths downstream. In examining Figure 15, the asymmetric behavior of the uncertainty is due to the non-symmetrical uncertainty of the contribution of artificial viscosity.
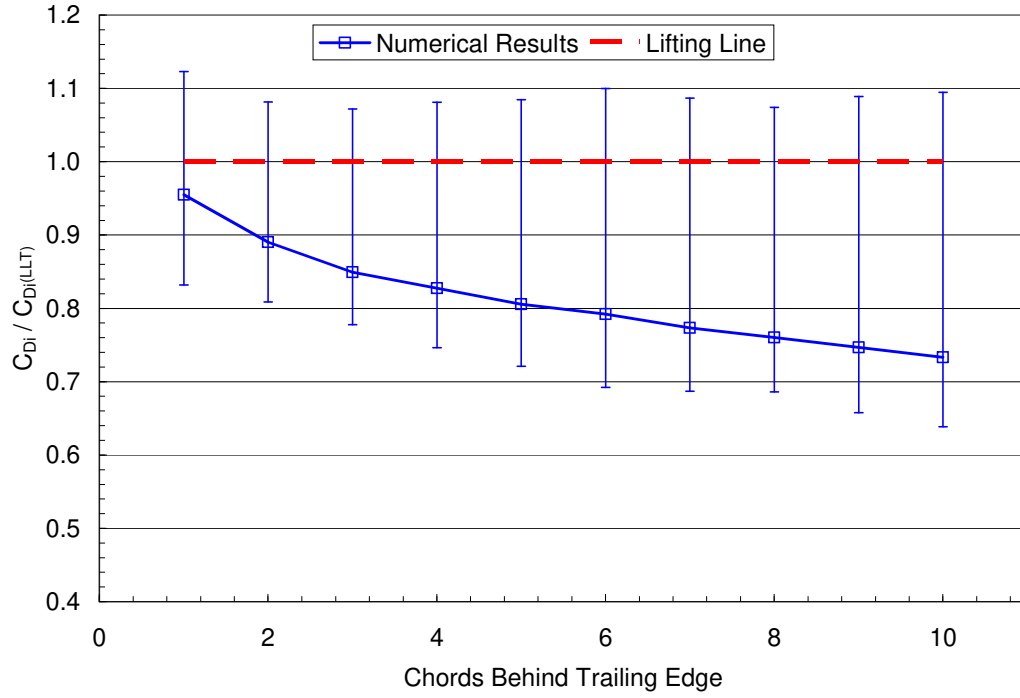
Figure 15. Results of Uncertainty Analysis

If one applies the correction suggested by Bourdin [6] and Van der Vooren [19], the "irreversible correction" mentioned above, for the irreversibilities brought on by artificial viscosity, this asymmetric uncertainty contribution will be reduced significantly, thereby reducing the total uncertainty of the induced drag calculation.

CHAPTER 7

CONCLUSIONS

A systematic approach was followed throughout this work. A technique was developed for extracting span-wise lift distribution. A lifting line code was written to handle the theoretical computations as well as comparison of the results and the researcher and code were verified against a theoretical baseline. Computational fluid dynamics (CFD) numerical results for an untwisted, finite rectangular wing (NACA 0012, AR = 6.7) using no flap deflections were compared against theoretical lifting line results and were shown to have satisfactory agreement with a maximum deviation of only 2.4% over the wing span.

Inaccuracies associated with the common surface integral method of calculating drag as well as its inability to provide a phenomenological breakdown into physical drag components (lift induced drag, wave drag, viscous drag) prompted the implementation of a far-field wake integral method. Several modifications to a classical Trefftz plane analysis were explored to minimize spurious drag with the eventual goal of yielding results that are independent of downstream position of analysis.

For a prediction to prove useful at the design stage it needs to be validated and its errors quantified. With this in mind, an initial grid convergence index (GCI) study was completed within the scope of an uncertainty analysis and served as an attempt to quantify the uncertainty associated with grid convergence and other related issues. A root-sum-square method was used to combine the effects of individual contributing

uncertainties and provide an estimate of total uncertainty with respect to the calculation of induced drag.

CHAPTER 8

FUTURE WORK

The next step of this research project is to continue to study and implement the "irreversible correction" suggested by Bourdin [6] and Van der Vooren [19]. Not only will the successful implementation of such a method reduce the total uncertainty of the predicted induced drag, but it will provide independency to the downstream location of the interrogation plane. With the global objective of the project being to achieve a closed loop abstract control system by coupling flow solver code with a structural optimization program in a design capable environment, this independency of downstream location is critical. Once the control loop is closed, the manipulation of multiple virtual trailing edge control surfaces will allow optimization of the lift distribution for specific needs, namely minimizing induced drag.

REFERENCES

[1]Sanders, B., Eastep, F., Forster, E., "Aerodynamic and Aeroelastic Characteristics of Wings with Conformal Control Surfaces for Morphing Aircraft," *J. Aircraft*, Vol. 40-1, 94-9.

[2]Kolonay, R., Eastep, F., "Optimal Scheduling of Control Surfaces on a Flexible Wing to Reduce Induced Drag," AIAA Paper 2004-4362, September 2004.

[3]Bourdin, P, "Numerical Predictions of Wing-tip Effects on Lift-induced Drag," ONERA – Applied Aerodynamics Department. BP72, 92322 Châtillon Cedex, France. ICAS 2002 Congress.

[4]Anderson Jr., John D., *Fundamentals of Aerodynamics*, 2nd ed., McGraw-Hill, New York, 1984 Chap 5.

[5]Smith, S.C., "A Computational and Experimental Study of Nonlinear Aspects of Induced Drag," NASA TR-3598, February 1996.

[6]Bourdin, P., "Planform Effects on Lift-induced Drag," AIAA Paper 2002-3151, June 2002.

[7]Kroo, I, "Drag Due to Lift: Concepts for Prediction and Reduction," *Annu. Rev. Fluid Mech.* 33:587:617, 2001.

[8]Nikfetrat, K., van Dam, C.P., Vijgen, P.M.H.W., Chang, I.C., "Prediction of Drag at Subsonic and Transonic Speeds Using Euler Methods," AIAA Paper 92-0169, Jan. 1992.

[9]Hunt, D., Cummings, R., Giles, M., "Wake Integration for Three-Dimensional Flowfield Computations: Applications," *J. Aircraft*, Vol. 36-2, 366-73.

[10]Wong, K.J., Ayers, T.K., van Dam, C.P., "Accurate Drag Prediction – A Prerequisite for Drag Reduction Research," SAE Paper 932571, Sept. 1993.

[11]Smith, S.C., *A Computational and Experimental Study of Nonlinear Aspects of Induced Drag*. Ph.D. Dissertation, Dept. Aeronautics and Astronautics, Stanford University, Stanford, CA, June 1995.

[12]Amant, S., "Drag Prediction and Decomposition, From Wake Surveys and Calculations, in Subsonic Flows," AIAA Paper 2001-2446, June 2001.

[13]Eppler, R., "About Classical Problems of Airfoil Drag," *Aerospace Science and Technology*, 7, 289-97.

[14]Giles, M., Cummings, R., "Wake Integration for Three-Dimensional Flowfield Computations: Theoretical Development," *J. Aircraft*, Vol. 36-2, 357-65.

[15]Kusunose, K., "Drag Prediction Based on a Wake-Integral Method," AIAA Paper 98-2723, 1998.

[16]Cummings, R.,Giles, M., Shrinivas, G., "Analysis of the Elements of Drag in Three-Dimensional Viscous and Inviscid Flows," AIAA Paper 96-2482, 1996.

[17]Schmitt, V., Destarac, D., "Recent Progres in Drag Prediction and Reduction for Civil Transport Aircraft at ONERA," AIAA Paper 98-0137, 1998.

[18]Destarac, D., Lecture Notes.

[19]Van der Vooren, J., Slooff, J.W., "CFD-based Drag Prediction: State of the Art, Theory, Prospects," National Aerospace Lab, TP-1990-247, Aug. 1990.

[20]Figliola, R.S., Beasley, D.E., *Theory and Design for Mechanical Measurements*, 4th ed., Wiley, 2005.

[21]Freitas, C.J., Ghia, U., Celik, I., Roache, P., Raad, P., "ASME'S Quest to Quantify Numerical Uncertainty," AIAA Paper 2003-627, 2003.

[22]Roache, P. J., *Verification and Validation in Computational Science and Engineering*, Hermosa Publishers, Albuquerque, NM.

[23]Kline, S.J., Morkovin, M.V., Sovran, G., Cockrell, D.J., "Computation of Turbulent Boundary Layers – 1968 AFOSR-IFP-Stanford Conference, Volume 1," Dept. of Mech. Eng., Stanford University.

[24]Roache, P.J., Ghia, K.N., White, F., "Editorial Policy Statement on the Control of Numerical Accuracy," *J. Fluids Engineering*, Vol. 108-2.

[25]Roache, P.J., "Perspective: A Method for Uniform Reporting of Grid Refinement Studies," *ASME J. Fluids Engineering*, Vol. 116, 405-13, 1994.

[26]Strang, W., Tomaro, R., Grismer, M., "The Defining Methods of Cobalt$_{60}$: A Parallel, Implicit, Unstructured Euler/Navier-Stokes Flow Solver," AIAA Paper 99-16635, January 1999.

[27]Gottlieb, J., Groth, C., "Assessment of Riemann Solvers for Unsteady One-Dimensinoal Inviscid Flows of Perfect Gases," *J. Computational Physics*, 78:437-58, 1988.

[28]Bertin, J., Smith, M. *Aerodynamics for Engineers*, 3rd ed., Prentice Hall, Upper Saddle River, NJ, 1998, Chap. 7.

[29]Betz, A., "Ein Verfahren zur Direkten Ermittlung des Profilwiderstandes," *ZFM*, Vol. 16, 1925, pp. 42-44.

[30]American Society for Mechanical Engineers, *Test Uncertainty*, PTC 19.1, New York, 1988 and 2005.